Oxid Met (2016) 85:369–389
DOI 10.1007/s11085-015-9601-0

ORIGINAL PAPER

The Effect of High Temperature Thermal Cycling on Near-Surface Sulphur Partitioning in Gamma and Gamma Prime Phases and Its Implications on Sulphur Segregation in Coated Ni-Base Superalloys

N. D'Souza[1] · F. Liu[1] · S. Irwin[1] · A. Brown[2] · I. M. Edmonds[1] · D. S. Rickerby[1]

Received: 8 September 2015 / Revised: 16 November 2015 / Published online: 7 December 2015

Abstract Secondary ion mass spectrometry (SIMS) was used to study the near-surface segregation of sulphur during; (a) the thermal processing stages (diffusion annealing after application of Pt bond coat and after secondary ageing following subsequent deposition of the Y_2O_3-stabilised ZrO_2 top coat) and (b) thermal cycling in the Ni-base superalloy, CMSX4. In the thermal processing stages, an increased segregation of sulphur was observed within the upper regions of the Pt bond coat after diffusion annealing, while following secondary ageing, the sulphur segregation in this layer became heterogeneous with discrete pockets of enrichment ($\gg$1 ppm) and regions of depletion ($\ll$1 ppm). During thermal cycling, partitioning of sulphur occurred to the Pt-enriched γ' region characterised by the finger-like morphology, while examination of TBC spalled specimens showed significant depletion of sulphur within the substrate in the vicinity of the surface. The reservoir for sulphur-depletion within the substrate was definitively identified as the Pt-enriched γ' region. A quantitative method for the calculation of sulphur-segregation at the surface in terms of mono-layers is presented.

Keywords Sulphur surface segregation · Bond coat morphology · Thermal cycling · Secondary ion · Mass spectroscopy · Mono-layers

✉ N. D'Souza
neil.dsouza@rolls-royce.com

[1] Rolls-Royce plc, P.O. Box 31, Derby DE24 8BJ, UK

[2] Lucideon Ltd, Queens Road, Penkhull, Stoke-on-Trent, Staffordshire ST4 7LQ, UK

Introduction

Ni-base alloys have been developed in order to meet stringent demands in the hot-sections of gas turbine engines, where not only creep and fatigue strength, but also enhancement of their oxidation and hot corrosion properties is an important consideration [1]. As modern turbine engines have hotter gas temperatures, the provision of thermal insulation to the turbine blade surface is imperative. This takes the form of a thermal barrier coating (TBC) and therefore a further requirement for the superalloy substrate is compatibility with the TBC that it is required to support [2, 3]. Commercial TBC systems are of the overlay and diffusion types. The former are discrete in nature and of the type MCrAlY (with M being Ni or Co or both). They have little chemical interaction or inter-diffusion with the base alloy. The diffusion coatings are comprised of a multi-layered structure. It is comprised of typically [4]; (i) top coat comprising of an yttria-stabilised zirconia (YSZ) layer formed by electron beam physical vapour deposition (EB-PVD) and (ii) bond coat made by either electro-deposited platinum followed by an inter-diffusion heat treatment—the NiPt bond coat (Pt-diffused bond coat) or via electro-deposited platinum followed by aluminising and then accompanied by an inter-diffusion heat treatment—NiPtAl bond coat.

The primary function of the bond coat is to develop a thermally grown oxide (TGO), which is Al_2O_3 that serves to adhere the top coat to the bond coat/superalloy substrate. In general, the performance of the TBC system during thermal cycling is limited by the adhesion of the top coat. Accordingly, there are two avenues of research aimed at understanding the compatibility of single crystal alloys with the coatings placed on them;

(i) The failure modes of the TBC and micro-mechanisms involved—this is shown to originate at/close to the TGO/bond coat interface; the driving force which arises largely from the mismatch in thermal expansion coefficients of the constituent layers in the system [5–7],
(ii) The role of the substrate chemistry, which dictates the chemical reactions at the TGO/bond coat interface. This involves major alloying elements as well as minor (trace) elements.

Major Elements

Co is shown to be detrimental, where an increase in Co composition was shown to decrease TBC spallation life and was proposed to result from a decrease in interfacial toughness of the bond coat/Al_2O_3 interface [8]. This arises since Co partitions to γ phase that forms beneath the TGO, as Al is consumed to form the oxide. This can be overcome by increasing the Pt composition in the bond coat. Uphill diffusion (against the concentration gradient) occurs leading to increasing concentration of Al at the surface. Increasing Al concentration at the surface

suppresses the formation of the γ' denuded zone and consequently improves the oxidation resistance [9–11].

Minor Elements (The Role of Sulphur)

S, which occurs as a tramp element segregates to any free surface, specifically to cavities and voids that exist prior or those that develop during thermal cycling. Segregation of S at the surface reduces the interfacial energy and in turn leading to accelerated growth of these cavities [12, 13]. This has also been confirmed by experimental evidence, where reduced S levels (typically <1 ppm) in the bulk, has shown to result in a marked decrease in mass-loss associated with oxide spallation during thermal cycling [14, 15].

In this study the focus will be on the minor elements, i.e. the role of S. The segregation of S to the surface can arise from a number of factors.

In the case of thermodynamic considerations this is given by the Langmuir–McLean isotherm [16];

$$\frac{\theta}{1-\theta} \propto e^{-\frac{\Delta H}{RT}} \tag{1}$$

where θ is the surface coverage relative to saturation and ΔH is the enthalpy of segregation (−ve). Therefore, surface segregation increases with decreasing temperature. However, the kinetics of S migration to the surface is governed by diffusion from the bulk, which decreases with decreasing temperature. Therefore, the maximum segregation of sulphur must occur in an intermediate temperature range and in the case of Ni-base alloys the experimentally measured surface segregation of S was maximum at 870 °C [16].

Alternatively, S can be incorporated into the oxide if the oxide growth is controlled by anion (O^{2-}) diffusion. This arises during the formation of α-Al_2O_3 by internal oxidation. However, since there is an appreciable solubility of S within the oxide ($\sim$2 ppm), such a partitioning of S to the oxide would require segregation of S at an intact oxide/metal interface [17]. This view has been supported by recent calculations into the fracture stress of the S-enriched interface [18] derived from the work of adhesion of Al_2O_3 on Ni and NiAl, which is typically [0.5–0.7] J m^{-2} and which is reduced to 0.18 J m^{-2} corresponding to 0.1 mono-layers of S coverage [19, 20].

The segregation characteristics of S have been studied through two principal approaches. In the case of studies focused at the surface, this has been done using a novel in situ method termed as “scratch testing”. In ultra-high vacuum (UHV) by careful peeling of the oxide from the substrate surface, Auger electron spectroscopy (AES) can be used to analyse the exposed alloy surface on oxide-imprinted areas, where either the oxide had been in contact with the surface prior to the scratch or on the surface of interfacial voids [12, 21]. In the case of investigations within the substrate this includes;

Energy Dispersive Spectroscopy Using Scanning Transmission Electron Microscopy (STEM/EDS)

The segregation pathways of S were determined in a β-(Ni,Pt)Al bond coat deposited on AM1 alloy, i.e. at β/β grain boundaries and γ'/β, γ'/Al_2O_3 phase boundaries [22, 23].

Secondary Ion Mass Spectrometry (SIMS)

Back-sputtered SIMS was used to determine the S segregation profile in NiPt, NiAl and β-(Ni,Pt)Al bond coat deposited on AM1 alloy in complete TBC systems. Unlike in (a) where profiles were obtained within 0.1 μm (100 nm) from the surface, in this case segregation profiles were obtained up to 10 μm beneath the oxide in the bond coat [24].

Glow Discharge Mass Spectrometry GDMS)

S segregation in Pt–Al bond coats and the accompanying depth profiles in Ni-base superalloy substrates was measured from the near-surface region to nearly 100 μm into the substrate [25].

Despite such a comprehensive study of the segregation behaviour of S during thermal cycling, there still exist features that merit particular attention and the aim of this article is to elucidate these aspects in three key areas.

First, the segregation of S to the surface is provided by the reservoir within the bulk. A quantitative measure of the amount of S segregated at the surface can only be made by considering the loss of S at the near-surface within the substrate.

Second, the microstructure of the reservoir is comprised of γ and γ' phases. The solubility of S is different in γ and γ' phases and dependent on the chemical potential and on the Pt concentration. Therefore, the fraction of γ and γ' phases will determine the "effective" reservoir for S within the substrate.

Third, composition measurements using SIMS and GDMS studies have generally been limited to depth profiles and the data is at best only semi-quantitative (intensity is not directly proportional to concentration). Further, the reliability of the depth calibration of a depth profile is based on having either a well calibrated sputtering rate or a direct measurement of crater depth. If the sample of interest contains surface oxide and/or surface layers which are compositionally different from the substrate alloy then accurate depth calibration is complex due to sputter rate differences between layers.

These factors have been systematically addressed in this study. The SIMS method is adopted, but instead of depth profiles, cross-sectional images are considered which provide a larger field-of-view over the depth of interest and where the measurements can be directly correlated with the microstructure. The use of cross-sectional SIMS imaging provides a convenient method for assessing relative changes in key elemental concentrations (e.g. sulphur) over the microstructural regions of interest within the sample. This is achieved by generation of retrospective

line-scans for the key elements from the stored image data. The additional inclusion of a range of suitably calibrated standards within the analytical protocol also provides a firm basis for assessing quantitative changes in e.g. sulphur concentration across the microstructure. It should be noted at this point that the intention of this paper is to provide a working method for the *approximate* assessment of changes in sulphur concentration across microstructural and compositional boundaries within the substrate, but at the near-surface. We do not measure the segregation of sulphur at the surface above the substrate.

Experimental Procedures

The 2nd generation Ni-base superalloy, CMSX-4® of nominal composition (wt%); Ni–5.6Al–9.6Co–6.4Cr–0.6Mo–3Re–6.5Ta–1Ti–6.4 W, S–0.3 ppm, was used. Single crystal turbine blades were produced via a state-of-the-art investment casting process followed by directional solidification, where the <001> crystal axis was within 10° from the blade-axis. The as-cast micro-segregation was subsequently eliminated by solution heat treatment in an Ar atmosphere. The blades were heated using a ramp cycle up to 1310 °C and then an isothermal hold followed by a rapid gas fan quench, where the non-equilibrium eutectic phases were dissolved and long-range compositional homogeneity was achieved. This was then followed by a primary ageing cycle in an Ar atmosphere at 1140 °C for 2 h followed by a rapid gas fan quench. After heat treatment, the surface of the blades was grit-blasted and subsequently vibro-barrelled to produce a fine surface finish. The aerofoil was sectioned into cross-sections and these cross-sections were rinsed thoroughly with cold water to remove any adherent processing residue and ultra-sonically cleaned. The bond coat was applied by electro-plating up to a 10 μm Pt layer followed by a diffusion heat treatment at 1150 °C for 1 h in Ar atmosphere. After annealing, the aerofoil surfaces were grit-blasted, pre-oxidised in vacuum and a ceramic layer of ZrO_2–8 wt% Y_2O_3 was deposited by electron beam physical vapour deposition (EB-PVD). This was then followed by heat treatment at 1100 °C for 1 h in Ar atmosphere followed by the secondary ageing cycle at 870 °C for 16 h and then rapidly quenched. Finally, the aerofoil sections underwent cyclic oxidation in air at 1190 °C. Each cycle consisted of 3 h dwell at 1190 °C, after which the samples were removed from the furnace and allowed to cool in air to room temperature. Thereafter, the test sections were immersed in or sprayed with water in order to displace any bond coat and top coat that had previously spalled off the substrate. All coating processes were carried out at Turbine Surface Technologies Ltd (TSTL), Nottingham, UK.

All scanning electron microscopy (SEM) analyses were performed using a dual beam (FEI Nova 600 nanolab) scanning electron microscope. Back-scatter electron images (BEI) were collected using a retractable solid-state back-scatter detector using high (20 kV) and low (5 kV) electron beam accelerating voltages; the images collected at lower voltages possessed increased grain channelling contrast, whilst those at the higher voltage possessed increased compositional contrast. Chemical

analysis was undertaken in this system at 20 kV using a 50 mm^2 Octane Silicon Drift Detector (SDD) from EDAX. A beam voltage of 20 kV with a current of 6.6 nA was used. The working distance (WD) varied between 5 and 10 mm.

The secondary ion mass spectrometry (SIMS) analyses were conducted using a CAMECA IMS 4f instrument. The aerofoil cross-sections were mounted on standard sample holders after sputter coating with a thin Au layer to prevent excessive charging during analysis. Images for the key metallic species, e.g. Al, Cr and Pt were obtained in positive secondary ion mode using a 15 keV O_2^+ primary ion beam. For S and O detection, images were acquired in negative secondary ion mode with a 10 keV Cs^+ primary ion beam. The mass spectrometer was set to a mass resolution of $\sim$2000 M/dM, in order to adequately separate $^{32}S^-$ from the isobaric $^{16}O_2^-$. Images were typically acquired from 100 μm × 100 μm and sometimes 250 μm × 250 μm areas.

Results and Discussion

Near-Surface Sulphur Segregation Before Thermal Cycling

After Platinum Electro-Plating and Diffusion Annealing (1150 °C/1 h)

Figure 1a–d are ion images obtained from an aerofoil cross-section following electro-plating with Pt and annealing at 1140 °C for 1 h. The composition profiles (expressed as intensity) across the cross-section, but restricted to the substrate and commencing close to the surface were determined along bands rather than as line-scans, where the compositions were averaged across the width of the band. The widths and positioning of the vertical bands are indicated in Fig. 1d.

The composition profile along a typical band is presented in Fig. 2 and corresponds to band C. The following observations can be made.

Figure 1c shows a Pt-enriched layer—the upper and lower limits of the Pt layer are indicated by the solid yellow and solid red curves respectively. It is also clear that the region between the solid red and dotted red curves corresponds to the substrate, since there is no enrichment in Pt that is observed. In Fig. 1b distinct regions are observed within this Pt layer, which is comprised of sub-regions 1, 2a and 2b. Region 2b is segregated in Cr (depleted in Al), while region 2a is depleted in Cr (enriched in Al) and partitioning of Cr in region 1 is intermediate, but nevertheless more segregated compared with the bulk. Finally in Fig. 1d, there is a marked variation observed in the partitioning behaviour of S within the Pt layer and substrate. S is markedly enriched in the upper Pt layer (within solid and dotted yellow curves), but depleted in the lower region (between dotted yellow and dotted red curves).

It can be unequivocally concluded that the region depleted in sulphur is only partly contained within the Pt-layer [2a + 2b], i.e. between the dotted yellow and solid red curves, while a portion (region 3) also exists outside of the Pt-layer within the substrate, i.e. between the solid red and dotted red curves. A clear demarcation

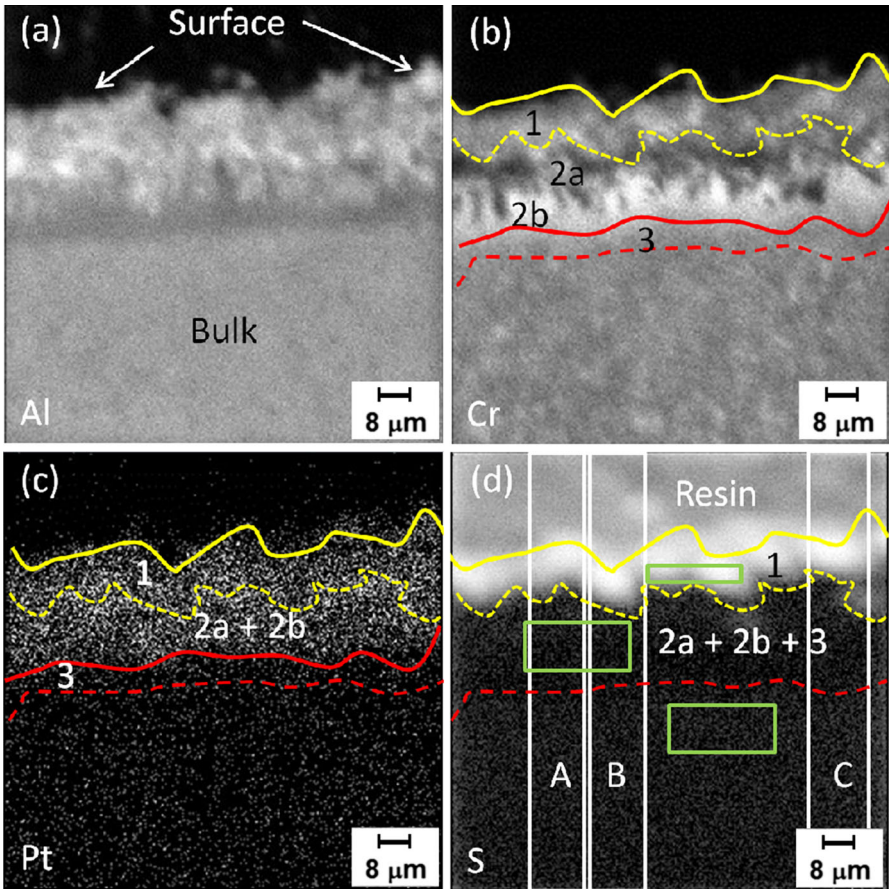

Fig. 1 Elemental SIMS maps from a transverse section of a sample after electro-deposition of Pt and subsequent diffusion annealing at 1140 °C for 1 h. **a** Al, **b** Cr, **c** Pt, **d** S

between the different regions [1, 2a + 2b + 3 and substrate] is difficult from Fig. 2, owing to the monotonic decrease in composition observed, rather than a sharp discontinuity across the interface. Therefore, the concentration as an intensity level was determined in each of the individual regions, corresponding to horizontal bands that are exclusively located within these sub-regions (Fig. 1d). The measured S concentrations are superimposed as solid black lines in Fig. 2. It can be observed that there exists a sharp discontinuity in S concentration between the different regions, where 1 = 217 units, [2a + 2b + 3] = 16.5 units and substrate = 25 units. Nevertheless, the overall concentration within each region obtained from the vertical scans is consistent with those measured in the horizontal scans. From Fig. 1, the approximate thicknesses of the different regions are as follows; Region 1 ~7 μm, [2a + 2b] ~ 15 μm [individual thicknesses of regions 2a and 2b is not reliable, owing to the "finger-like" morphology within 2a and hence more appropriate to

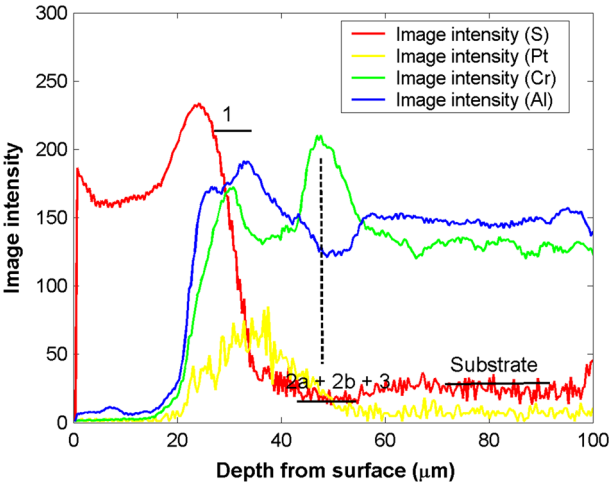

Fig. 2 Concentration profiles (intensity) along band scans showing segregation of Al, Cr, Pt and S from the surface into the substrate in a sample after electro-deposition of Pt and subsequent diffusion annealing at 1150 °C for 1 h (c.f. Fig. 1)

report a combined thickness]. Consequently, the total thickness of the Pt-enriched layer [1 + 2a + 2b] ~ 22 μm.

Figure 3a is a back-scattered electron image (BEI) that encompasses the region from where the SIMS map was collected and a higher magnification image corresponding to a portion of Fig. 3a is shown in Fig. 3b. The Al_2O_3 grit particles outline the original sample surface, where the layer above the grit constitutes the electro-plated Pt layer. From the Pt EDS map in Fig. 3c, it is clear that there is a distinct enrichment of Pt within the upper portion of the Pt-layer (above the grit-line). Moreover, there are distinct morphologies within the Pt layer, both above and below the grit-line.

Keeping the Numbering Consistent with Figs. 1 and 2;

- Above the grit-line, there are isolated islands (1a) and (1b) embedded within the Pt-enriched matrix.1a(at% :) Al = 19.1, Pt = 40.7, Ti = 0.8, Cr = 7.4, Co = 4.2, [Ta + W + Re] = 0.1b (at% :) Al = 14.6, Pt = 34.1, Ti = 1.5, Cr = 6.2, Co = 5.1, [Ta + W + Re] = 4.4.
- Below the grit-line, these islands (2a) are more profuse and occur as a "finger-like" morphology.

$$2a\ (at\%):\ Al = 13.2,\ Pt = 26.7,\ Ti = 1.9,\ Cr = 2.4,\ Co = 4.4,\ [Ta + W + Re] = 9.7$$

- There exists the region (2b) beneath the finger-like morphology, but within the Pt layer and segregated in Cr.

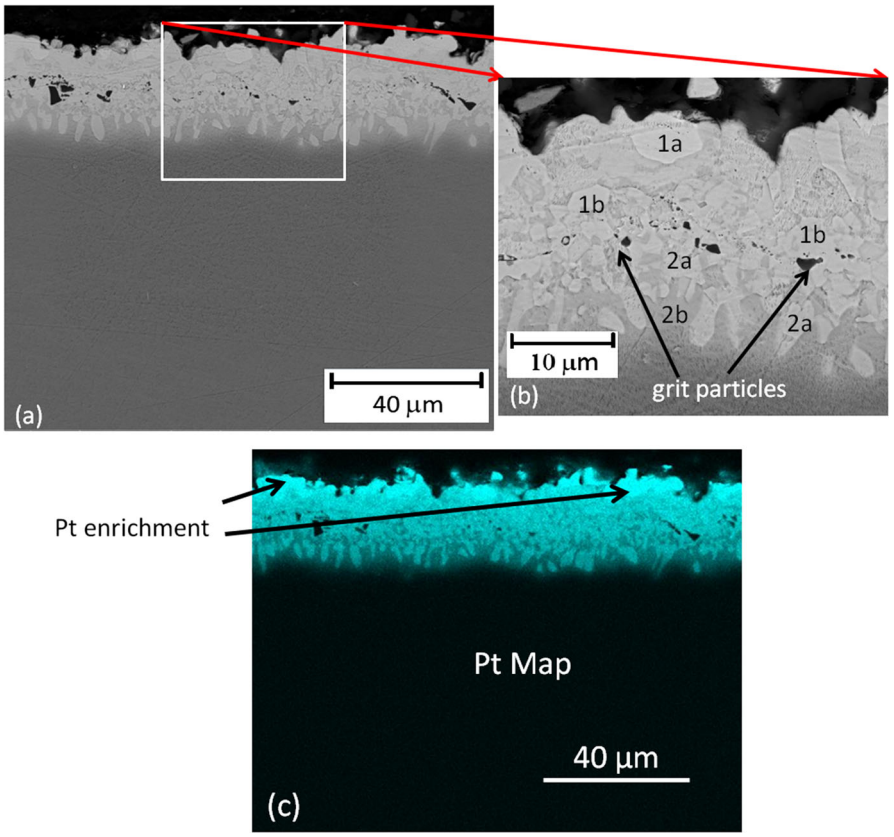

Fig. 3 Microstructure evolution in a sample after electro-deposition of Pt and subsequent diffusion annealing at 1140 °C for 1 h (c.f. Fig. 1). **a** Back-scattered electron image (BEI), **b** higher magnification image of a portion in **a**, **c** Energy dispersive spectroscopy (EDS) map for Pt

$$\begin{aligned} 2\text{b (at\%)}: \ \text{Al} &= 4.4, \ \text{Pt} = 11.9, \ \text{Ti} = 0.6, \ \text{Cr} = 6.7, \\ \text{Co} &= 10.6, [\text{Ta} + \text{W} + \text{Re}] = 8.2 \end{aligned}$$

The following conclusions can be made;

There is a marked uphill diffusion of Al from the substrate to the Pt deposited region. This is because diffusion is driven by difference in chemical potential (μ); $\mu_{Al}^{Pt(\gamma')} < \mu_{Al}^{\gamma}$, where the superscript refers to the Pt-enriched γ′ phase at the surface. The diffusion of Al therefore occurs from γ to Pt-enriched γ′ phase at the surface and consistent with other studies [26–30].

There is also re-distribution of sulphur arising within the Pt layer itself following an interaction with the substrate. The *increased* number of moles of sulphur in the upper Pt layer (region 1) is provided by the sulphur depleted from the substrate

beneath. This is manifested by the *decreased* number of moles of sulphur in the inter-diffused Pt layer in the substrate below the grit-line (region 3).

The segregation of S within the Pt layer; i.e. region 1 vis-à-vis regions 2a + 2b can only arise if; $\mu_S^{Pt+(\gamma')} < \mu_S^{Pt-(\gamma')}$. Here, Pt + (Region 1) and Pt-(Regions 2a + 2b) indicate increased and decreased Pt compositions corresponding to the outer and inner Pt surface layers respectively. During diffusion annealing therefore, the Pt concentration has a marked influence on the chemical potential of S. The lowering of the chemical potential of sulphur has also been reported in other systems as well; in MARM002 with a NiPtAl bond coat, sulphur has been shown to partition to Hf to form oxy-sulphide particles within the diffusion zone [31].

After Secondary Ageing (870 °C/16 h)

Figure 4a is a BEI that shows a cross-section following secondary ageing, which also corresponds to the regions from where elemental SIMS maps have been obtained. A higher magnification image is presented in Fig. 4b. Elemental EDS maps of Al and Pt and corresponding to Fig. 4a are presented in Fig. 4c and d, respectively. As in the case of electro-plating and diffusion annealing, the

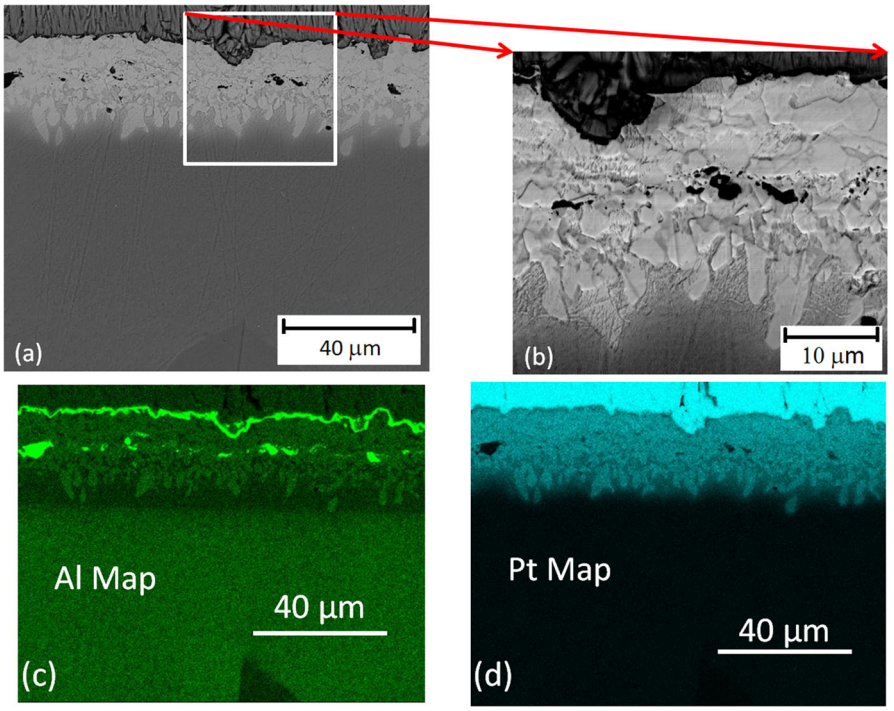

Fig. 4 Microstructure evolution in a sample after secondary ageing at 870 °C for 16 h. **a** Back-scattered electron image (BEI), **b** higher magnification image of a portion in **a**, **c** EDS map for Al, **d** EDS map for Pt

composition and morphology within the layers of the substrate in the vicinity of the surface were examined. In comparison to Fig. 3, the ingress of the Pt layer into the substrate during ageing is minimal ($\leq$3 μm). However, there is the occurrence of profuse "island" morphology within the Pt layer. There is also the distinct presence of the thermally grown oxide (TGO) at the interface between the Pt surface layer and the YSZ (TBC). This oxide is α-Al_2O_3. The mean composition within the Pt-enriched layer above and below the grit-line are summarised as;

Above the grit-line:

$$(\text{at}\%): \ \text{Al} = 14.3, \ \text{Pt} = 30.0, \ \text{Ti} = 1.17, \ \text{Cr} = 7.9, \\ \text{Co} = 6, [\text{Ta} + \text{W} + \text{Re}] = 3.0$$

Below the grit-line:

$$(\text{at}\%): \ \text{Al} = 15.0, \ \text{Pt} = 25.8, \ \text{Ti} = 1.7, \ \text{Cr} = 3.4, \\ \text{Co} = 4.4, [\text{Ta} + \text{W} + \text{Re}] = 8.0$$

Comparing this with the composition evolution after diffusion annealing, there is primarily inward diffusion of Pt from the outer to inner Pt-layer and the concomitant disappearance of the prominent outer Pt-enriched layer (region 1 in Fig. 1). The difference in Al composition on the other hand is within the measurement accuracy.

Figure 5a and b are corresponding ion images for Al and S respectively. The composition profiles were measured along vertical bands and the widths and positioning of the bands are indicated in Fig. 5b. The composition profile (intensity) along a typical band is presented in Fig. 6 and corresponds to band B. The thickness of the Pt layer, i.e. keeping the same terminology as before [1 + 2a + 2b] was 25 μm. However there is a significant heterogeneity in the distribution of S, thereby indicating that the band-scan is too coarse and does not have the spatial resolution for interpreting the partitioning of S. The thickness of the Al depleted layer [region 3] in the substrate is $\sim$6 μm. To analyse this heterogeneity more accurately,

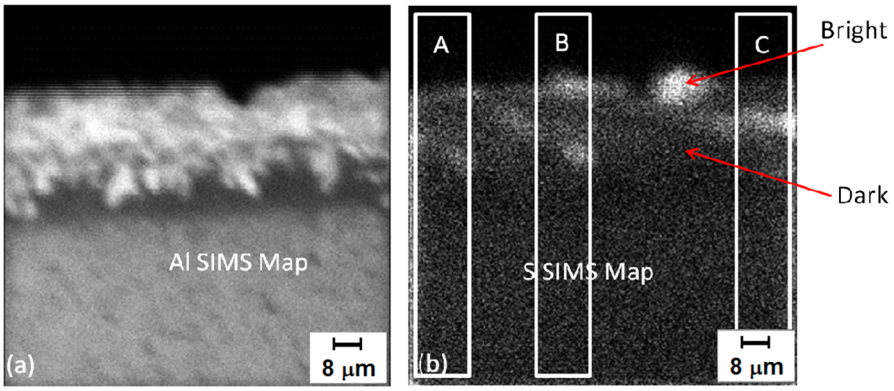

Fig. 5 Elemental SIMS maps from a transverse section of a sample after secondary ageing at 870 °C for 16 h (c.f. Fig. 4). **a** Al, **b** S

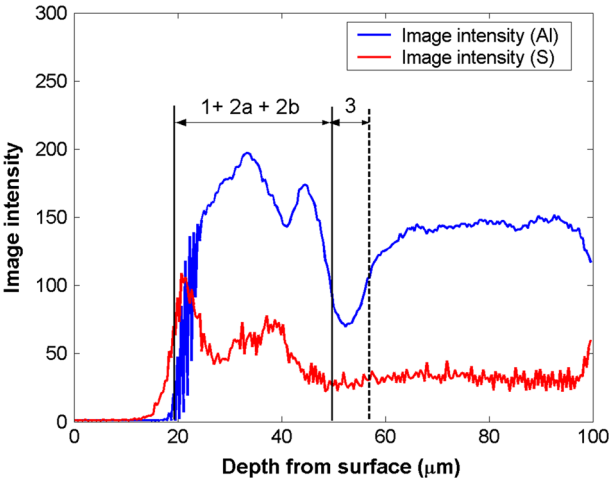

Fig. 6 Concentration profiles (intensity) along band scans showing segregation of Al, and S from the surface into the substrate in a sample after secondary ageing at 870 °C for 16 h (c.f. Fig. 5)

quantitative SIMS was carried out within regions in the Pt layer and only the extremities in composition were calculated. In Fig. 5b, for the very bright regions, S ~3.4 ppm (using the method described in the Appendix).

There is clearly a significant change in the partitioning of S observed at the near-surface following the secondary ageing treatment. In fact such a heterogeneous S distribution has been reported, albeit during cyclic oxidation of the Ni-base alloy, AM1 at 1100 °C and having a NiPtAl bond coat, unlike the NiPt bond coat in our experiments [24]. 200–650 nm S-rich zones surrounded by S-depleted matrix were detected using back-sputtered GDMS within 7 μm from the surface. In the present experiments it was not possible to ascertain if the localised S distribution was associated with similar segregation of other elements (such as Pt) [32], since analysis of regions with such sizes (~2 μm) is limited by the achievable spatial resolution. Nonetheless, it is important to emphasise the presence of such segregated and depleted zones for S within the Pt surface layer following secondary ageing and prior to thermal cycling. The existence of an inherent defect population within the thermally grown oxide during the processing stages, leads to S segregation, which is driven from the bond coat [33].

Near-Surface Sulphur Segregation Within the Substrate During Thermal Cycling (1190 °C/3 h and Cool)

During thermal cycling two situations can arise; first, there is the diffusion of S to the existing cavities, cracks and pores as well as to the surface, the latter accentuated if the oxide has spalled, even though segregation of S does occur to intact surfaces. Second, if spallation does occur, most of the sulphur at the surface is adsorbed from the environment. In order to delineate the contribution of the latter from that of S diffusing from the bulk, the substrate has to be examined rather than the surface.

The loss of S within the substrate in the vicinity of the surface then constitutes the reservoir. At the same time there is also the diffusion of Pt from the bond coat into the substrate and this also results in a changing evolution of S within the surface layers, since the partitioning of S in γ and γ' phases is not the same. Accordingly, two characteristic regions were considered that were representative of thermal cycling;

Region 1—The TBC is adherent (earlier cycles), but there exist localised cavities and voids at the interface, which have formed during thermal cycling [34].

Region 2—The TBC has spalled (latter cycles) and spallation is adhesive in nature occurring at the bond coat/oxide interface and thereafter producing a "free surface" where subsequent transient oxidation occurs.

These regions will be now considered in some brevity.

Region I

Figure 7a and b are ion images for Al and S respectively. The composition profiles were measured across bands and the widths and positioning of the bands are indicated in Fig. 7b. The composition (intensity) profile along a typical band is presented in Fig. 8 and corresponds to band A. Figure 9a is a BEI showing the evolution of the microstructure across a cross-section and the Al and Cr EDS maps are presented in Fig. 9b and c, respectively. The following observations can be made;

There is the growth of Al_2O_3 with final thickness $\sim$5 μm. The growth of Al_2O_3 is accompanied by loss of Al and in the absence of long-range diffusion, this leads to the formation of the γ' denuded zone, with thickness $\sim$2.5 μm having composition;

$$(\text{at}\%): \ \text{Al} = 8.0, \ \text{Pt} = 8.7, \ \text{Ti} = 1.1, \ \text{Cr} = 11.0,$$
$$\text{Co} = 11.0, [\text{Ta} + \text{W} + \text{Re}] = 6.5$$

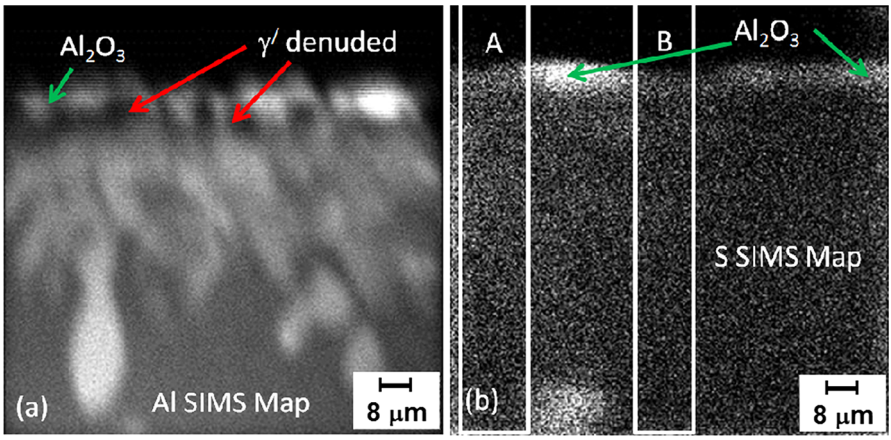

Fig. 7 Elemental SIMS maps from a transverse section of a sample after intermediate thermal cycling (each cycle is 1190 °C for 3 h). No spallation of the TBC was observed. **a** Al, **b** S

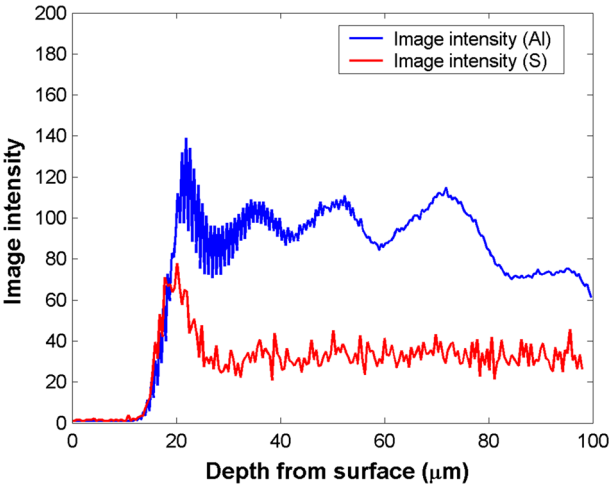

Fig. 8 Concentration profiles (intensity) along band scans showing segregation of Al, and S from the surface into the substrate in a thermally cycled sample (c.f. Fig. 7)

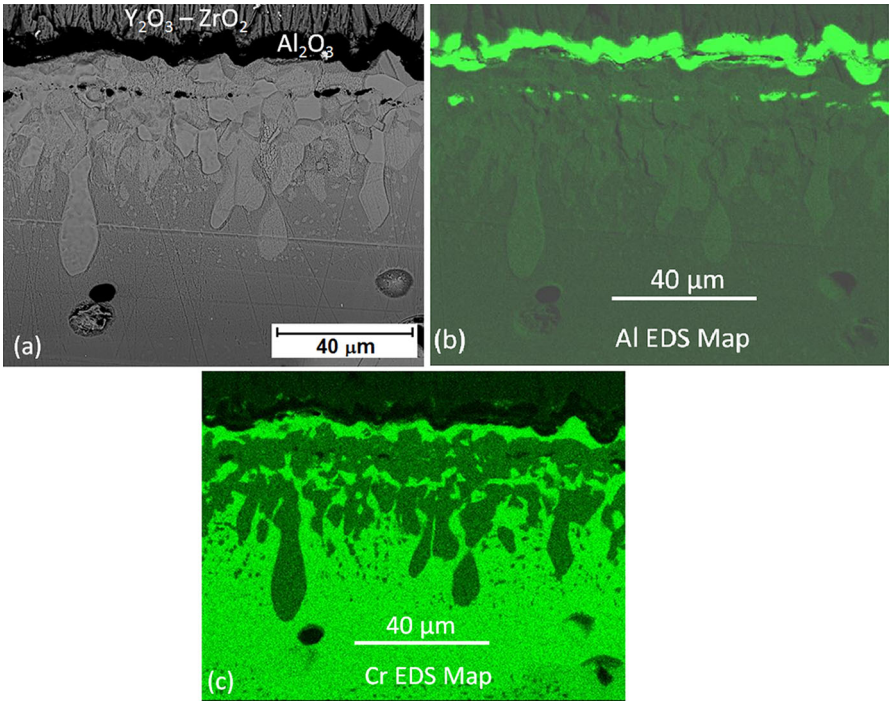

Fig. 9 Microstructure evolution in a sample after intermediate thermal cycling (c.f. Fig. 7). **a** Back-scattered electron image (BEI), **b** EDS map for Al, **c** EDS map for Cr

There is also partitioning of S to the oxide and therefore must be consumed from within the substrate. In the case of anion, O^{2-} diffusion controlled growth of α-Al_2O_3, this occurs via "interface sweeping", while during growth of transitional [γ, δ, θ]-Al_2O_3, this occurs across the alloy/oxide interface [12]. The net S consumed from the substrate can be obtained from a mass balance if the solubility of S in the oxide is known. Per unit area (A = 1 cm^2), this can be written as;

$$[C_S t_{Oxide} \rho_{Oxide}] = 1.95 \times 10^{-5} \text{g cm}^{-2}, \text{ where } C_S \approx 1\text{ppm [21] and } \rho_{Oxide} = 3.9 \text{ g cm}^{-3}.$$

Diffusion of Pt occurs during subsequent thermal cycling. Since there is greater solubility of Al within the Pt-enriched γ', growth of the Pt-layer is associated with surrounding Al-depleted (Cr-enriched) regions. Such "dark" regions are observed in the Al SIMS map in Fig. 7a between the Pt-fingers and corresponds to the "troughs" within the band-scan for Al in Fig. 8. Clearly there is a two-fold reduction in the Pt composition compared with the secondary aged condition

$$\text{Pt-fingers (at\%)}: \text{ Al } = 15.1, \text{ Pt } = 12.3, \text{ Ti } = 2.4, \text{ Cr } = 3.1, \text{ Co } = 6.0$$

$$\text{Between Pt-fingers : (at\%) : Al} = 8.2, \text{ Pt } = 8.6, \text{ Ti } = 1.1, \text{ Cr } = 10.7, \text{ Co } = 10.8$$

The partitioning of S between [Pt-enriched] γ' regions and the γ' denuded region between the Pt-fingers can be observed in the sinusoid-type pattern for the S-plot which follows the Al profile. There exists a preferential partitioning of S to Pt-enriched γ', although this is not as prominent as in the diffusion annealed condition. From the S composition profile it was not possible to unequivocally detect loss of S within the substrate during thermal cycling, which would arise when S segregates to voids, cracks and pores and to the "intact" surface".

Region II

Figures 10a and b are corresponding ion images for Cr and S respectively. In this case, TBC spallation has occurred at the oxide/bond coat interface. In the absence of the TBC and oxide, it is advisable to consider the Cr SIMS map to demarcate the surface of the sample. The Al SIMS map is not preferred owing to the presence of the γ' denuded layer at the surface, which appears dark in the SIMS map and therefore unable to delineate the sample surface. TBC spallation has occurred at the bond coat/oxide interface. During subsequent oxidation of the γ' denuded layer (Fig. 10c, d) in ongoing thermal cycling, NiO and other transient oxides (spinels) form and which subsequently spall during cooling and migration of S to the surface is significantly enhanced during each successive cycle [35]. However when spallation has occurred, most of the S at the surface is that adsorbed from the environment and to discount this contribution the amount of S within the substrate at

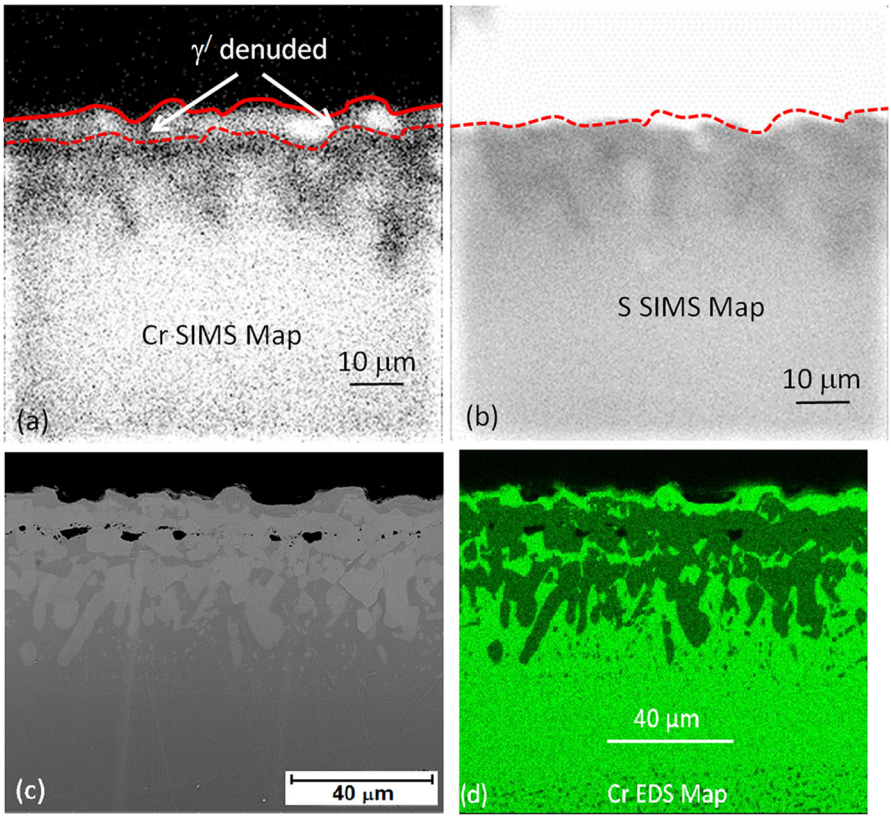

Fig. 10 Elemental SIMS maps from a transverse section and microstructure evolution in a sample after intermediate thermal cycling. The TBC has spalled at the oxide/bond coat interface. **a** Cr SIMS map, **b** S SIMS map, **c** Back-scattered electron image (BEI), **d** EDS map for Cr

the near-surface is measured. Any loss in S within these layers is evidence of S segregation to the surface, or to flaws during thermal cycling.

There is a distinct depletion of S from within the finger-morphology enriched in Pt, which is evident when comparing the Cr and S SIMS maps. Therefore, it follows that the reservoir from where S is depleted within the substrate constitutes the Pt-enriched γ' layer.

From Figs. 8 and 9 (Region I)

$C_S^{Bulk} = 0.3$ ppm. Since S segregates to Pt-enriched γ' layer, $C_S^{Pt(\gamma')} \approx 0.35$ ppm $> C_S^{Bulk}$. From the measured composition in Region 1, we obtain $\rho \approx 10\,\mathrm{gcm}^{-3}$, which is calculated from the known composition using a commercially available software package, JMatPro^{TM} that uses the thermodynamic database, Ni-Data [36].

From Fig. 11 (Region II)

The composition of S within the Pt-enriched γ' layer (reservoir) was measured using the quantitative SIMS method and is within the detection limit of 0.1 ppm. The initial composition corresponded to the nominal 0.3 ppm.

The "volume of the region comprising the finger-morphology is, V (cm^3).

S also partitions to Al_2O_3 (at bond coat/TBC interface) and let $t^{Al_2O_3}$ be the oxide thickness (in cm) when spallation has occurred and let A be the interfacial area (cm^2). $\rho_{Al_2O_3} = 3.9\,gcm^{-3}$ and $C_S^{Al_2O_3} \approx 1$ ppm [21].

It is important to note that numerous defects, such as cracks, separations, pores in alumina exist after electro-plating, diffusion annealing and secondary ageing. However, we have shown that S loss from the substrate to these regions is localised, as in the SIMS maps for S in Figs. 1d and 5b corresponding to diffusion annealing and secondary ageing respectively. In fact even after initial thermal cycling a similar situation is encountered, Fig. 7b. Significant depletion of S from the substrate is only observed in the latter stages of thermal cycling when the oxide has spalled, Fig. 11b. Since the reservoir corresponds to the layers of the substrate in the vicinity of the surface, the measured S depletion will be representative of S lost to the surface and other defects within the bond coat. This effectively precludes S from the environment that resides on the spalled surface. An approximate analyses for the S segregated at the surface is mon-layers can be done in this case.

Mass of S within the Pt-enriched γ' region in earlier stages of thermal cycling $= M_S^1(\text{before cycling}) = C_S^{Pt(\gamma')} V\rho = \left[3.5 \times 10^{-6} V\right] g$

Mass of S within region after latter stages of thermal cycles $= M_S^2(\text{after thermal cycles}) = c_S^{Pt(\gamma')} V\rho = \left[1 \times 10^{-6} V\right] g$

Mass of S within $Al_2O_3 = M_S^3(\text{in } Al_2O_3) = c_S^{Al_2O_3} t^{Al_2O_3} \rho^{Al_2O_3} A = [3.9 \times 10^{-6} t^{Al_2O_3} A] g$

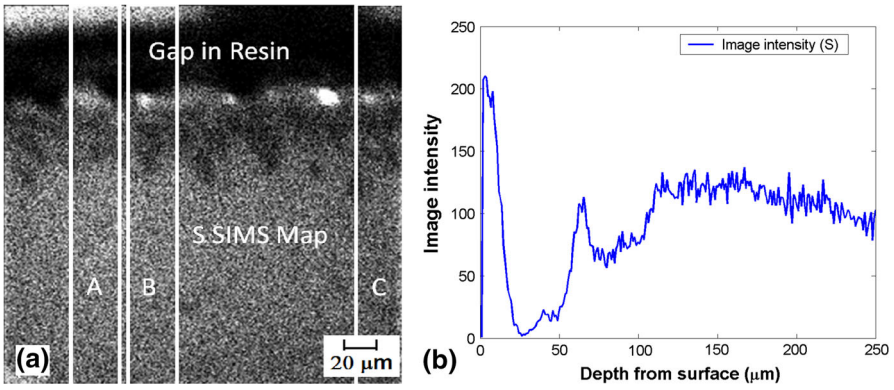

Fig. 11 **a** Sulphur SIMS maps from a transverse section of a sample after several stages of thermal cycling. The TBC has spalled at the oxide/bond coat interface. **b** Concentration profiles (intensity) along band scans showing segregation of S to the surface and corresponding depletion in the substrate

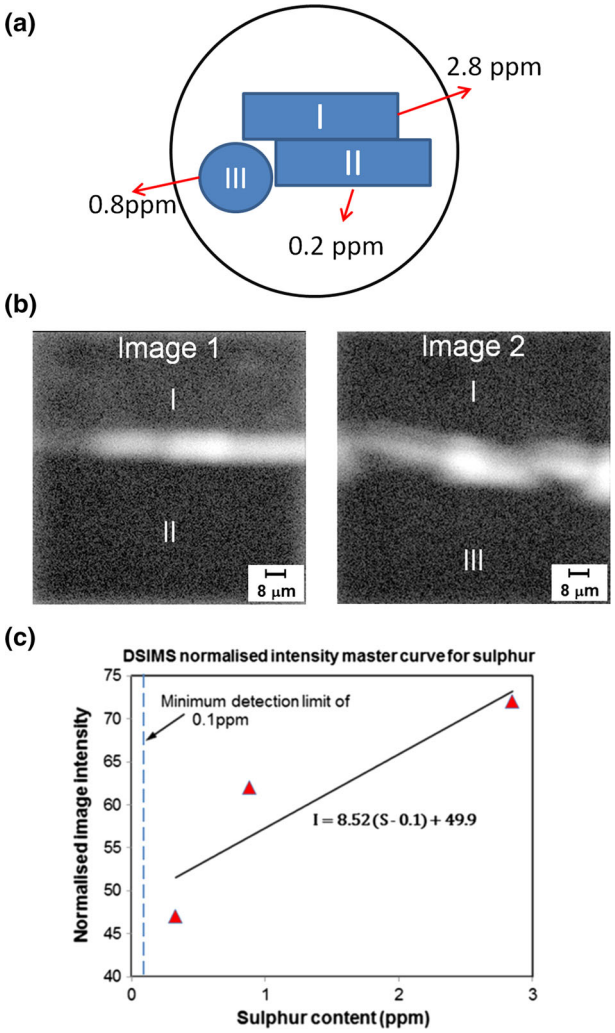

Fig. 12 Secondary Mass Ion Spectroscopy (SIMS) based method for calculating sulphur concentration. **a** Schematic showing positioning of reference samples on mount, **b** SIMS map for sulphur from reference samples, **c** calibration curve for reference samples

Therefore, S segregating to "free surface" during thermal cycling $= [M_S^1 - (M_S^2 + M_S^3)] = \left[2.5 \times 10^{-6} V\left(1 - 1.56 t^{Al_2O_3} \frac{A}{V}\right)\right] g = 4.71 \times 10^{16} V\left(1 - 1.56 t^{Al_2O_3} \frac{A}{V}\right)$ atoms

If n = number of mono-layers of S and if N_m = number of metal sites per interfacial area $\sim 1.55 \times 10^{15}$ atom cm^{-2};

$$n = \frac{4.71 \times 10^{16} t^{\text{Pt enriched}\gamma'}\left(1 - 1.56 t^{Al_2O_3}\frac{A}{V}\right)}{1.55 \times 10^{15}} = 30.4 t^{\text{Pt enriched}\gamma'}\left(1 - 1.56 t^{Al_2O_3}\frac{A}{V}\right) \quad (5a)$$

If thermal cycling is continued, there is an increasing segregation of S to the surface. This is seen in Fig. 11a, which is an ion image for S and which shows a complete depletion of S from within the Pt-enriched γ' finger-morphology. Once again it is clear that the reservoir for S corresponds to the Pt-enriched layer, just like in the intermediately thermally cycled region 2. In this case, the number of monolayers segregating to the surface is given by ($M_S^2 = 0$);

$$n' = 42.5 t^{\text{Pt enriched}\gamma'}\left(1 - 1.11 t^{Al_2O_3}\frac{A}{V}\right) \quad (5b)$$

The reservoir for S is therefore dominated by the Pt-enriched γ' layer with a limited contribution from the γ-phase. The extent of growth of this layer into the substrate is governed by the diffusivity of Pt in Ni. In the absence of the Pt layer, segregation of S to the surface will be driven by volume diffusion through both γ and γ' phases, as in the case H_2 annealing, which is a common method of de-sulphurising [15, 37]. It is also worth emphasising that other segregation pathways exist, such as grain boundaries, and these would be expected to be more potent than volume diffusion at thermal cycling temperatures $\sim$1150 °C, but this does not form the emphasis in this article [22].

The implications of this study clearly justifies the approach of reducing the S content in the alloy to reduce the adhesive failure of TBC's that occurs at the oxide/bond coat interface and which forms one of the possible failure mechanisms. Empirical lifing methods based on a Weibull approach and using ceramic spallation data obtained through furnace cyclic testing, show that the fraction of the population associated with a marked increase in ceramic spallation life in fact corresponds to a bulk composition of sulphur <1 ppm.

Conclusions

(1) Secondary Ion Mass Spectrometry (SIMS) was used to study the near-surface segregation of sulphur during thermal processing and subsequent thermal cycling in the Ni-base superalloy, CMSX4.

(2) During thermal processing:

   a. An increased segregation of sulphur was observed within the upper regions of the Pt bond coat after Pt electro-plating and diffusion annealing, with concomitant depletion within the substrate. This arises from a lower chemical potential of sulphur with increasing concentration of Pt.

b. After secondary ageing, the sulphur segregation in this layer became heterogeneous with discrete pockets of enrichment ($\gg$1 ppm) and regions of depletion ($\ll$1 ppm).

(3) During thermal cycling, sulphur partitions preferentially to the Pt-enriched γ' region having a finger-like morphology.
(4) The reservoir for sulphur-depletion at the near-surface within the substrate was defined by the Pt-enriched γ' region. Therefore, the size of the reservoir is determined by the extent of ingress of the Pt-enriched finger-like morphology into the substrate.
(5) An approximate method for the sulphur-segregation index at the surface in terms of mono-layers was presented.

Appendix

Methodology for quantitative calculations using cross-section SIMS maps:

The engineering mathematics software Matlab was used to process and analyse the SIMS generated elemental maps for a quantitative analyses of sulphur. First, the acquired data was stored as TIFF file formats with a logarithmic and linear grey scale corresponding to secondary ion count levels, scaled within each separate image The TIFF images were imported into the Image Processing Toolbox of Matlab and converted into 16-level grayscale intensity maps in the form of 250×250 pixel matrices. The intensity of each pixel can be related to its composition level (ppm wt.) via a calibration curve. The calibration curve for sulphur was obtained by considering samples that were machined from the bulk of castings. Figure 12a is a schematic diagram that shows the spatial location of the three samples (I, II and III) on the mount for SIMS calibration measurement and the corresponding S concentrations in ppm are indicated [independently measured using glow discharge mass spectrometry (GDMS) on polished surfaces against a sulphur standard (SRM1244-2012) certified by the National Institute of Standard and Testing (NIST)]. The following best-fit equation corresponds to the calibration curve;

$$\mathrm{I} = 8.52(\mathrm{S} - 0.1) + 49.9 \tag{6}$$

where I is the pixel intensity and S is the sulphur concentration in ppm. For a minimum detection limit of $\sim$0.1 ppm, this gives a background intensity of 49.9. Consequently, for a measured intensity corresponding to a given micro-structural feature in the SIMS map; an estimate for the sulphur concentration can be made from the calibration curve. It is worth noting that the raw image intensity can be affected by the "scaling" factor applied while producing a SIMS map. Therefore, the two SIMS maps in Fig. 12b have been normalised against the common region (sample I) from which Fig. 12c is obtained.

References

1. D. K. Das, *Prog. Mater. Sci.* **58**, 151–182 (2013).
2. C. G. Levi, *Curr. Opin. Solid State Mater. Sci.* **8**, 77–91 (2004).
3. A. G. Evans, D. R. Mumm, J. W. Hutchinson, G. H. Meier, and F. S. Pettit, *Prog. Mater. Sci.* **46**, 505–553 (2001).
4. T. Strangman, D. Raybold, A. Jameel, and W. Baker, *Surf. Coat. Technol.* **202**, 658–664 (2007).
5. V. K. Tolpygo and D. R. Clarke, *Acta Mater.* **52**, 5115–5127 (2004).
6. V. K. Tolpygo and D. R. Clarke, *Acta Mater.* **52**, 5129–5141 (2004).
7. M. Y. He, J. W. Hutchinson, and A. G. Evans, *Acta Mater.* **50**, 1063–1073 (2002).
8. R. T. Wu and R. C. Reed, *Acta Mater.* **56**, 313–323 (2008).
9. B. A. Pint, *Surf. Coat. Technol.* **188–189**, 71–78 (2004).
10. P. Y. Hou and V. K. Tolpygo, *Surf. Coat. Technol.* **202**, 623–627 (2007).
11. Y. Zhang, B. A. Pint, J. A. Haynes, and I. G. Wright, *Surf. Coat. Technol.* **200**, 1259–1263 (2005).
12. P. Y. Hou, *Annu. Rev. Mater. Res.* **38**, 275–298 (2008).
13. H. J. Grabke, D. Weiner, and H. Viefhaus, *Appl. Surf. Sci.* **47**, 243–250 (1991).
14. J. L. Smialek, *Metall. Trans. A.* **22**, 739–752 (1991).
15. J. L. Smialek, *JOM* **52**, 22–25 (2000).
16. J. L. Smialek, D. T. Jayne, J. C. Schaeffer, and W. H. Murphy, NASA/TM-106734 (1994).
17. P.Y. Hou, K. Pruβner, D.H. Fairbrother, J.G. Roberts, and K.B. Alexander, *Scr. Metall.* **40**, 241–247 (1999).
18. H. E. Evans, *Oxid. Met.* **79**, 3–14 (2013).
19. E. A. A. Jarvis, A. Christensen, and E. Carter, *Surf. Sci.* **487**, 55–76 (2001).
20. K. M. Carling and E. A. Carter, *Acta Mater.* **55**, 2791–2803 (2007).
21. P. Y. Hou and K. Priimak, *Oxid. Met.* **63**, 113–130 (2005).
22. R. Molins, I. Rouzou, and P. Y. Hou, *Oxid. Met.* **65**, 263–283 (2006).
23. R. Molins and P. Y. Hou, *Surf. Coat. Technol.* **201**, 3841–3845 (2006).
24. T. Gheno, D. Monceau, D. Oquab, and Y. Cadoret, *Oxid. Met.* **73**, 95–113 (2010).
25. I. T. Spitsberg and K. Putyera, *Surf. Coat. Technol.* **139**, 35–43 (2001).
26. Y. Zhang, J. P. Stacy, B. A. Pint, J. A. Haynes, B. T. Hazel, and B. A. Nagaraj, *Surf. Coat. Technol.* **203**, 417–421 (2008).
27. Y. Zhang, D. A. Ballard, J. P. Stacy, B. A. Pint, and J. A. Haynes, *Surf. Coat. Technol.* **201**, 3857–3861 (2006).
28. Y. Zhang, B. A. Pint, J. A. Haynes, and I. G. Wright, *Surf. Coat. Technol.* **200**, 1259–1263 (2005).
29. W. Y. Lee, Y. Zhang, I. G. Wright, B. A. Pint, and P. K. Liaw, *Met. Mater. Trans. A* **29A**, 833–841 (1998).
30. D. S. Rickerby, United States Patent, US005667663(A) (1997).
31. D. S. Rickerby and P. Morrell, *Thermal Barrier Coatings II, Engineering Conferences International* (Kloster Irsee, Germany, 2007).
32. P. Y. Hou and K. F. McCarty, *Scr. Mater.* **54**, 937–941 (2006).
33. P. K. Wright and A. G. Evans, *Current Opinion in Solid State & Materials Science* **4**, 255–265 (1999).
34. H. M. Tawancy, A. I. Mohamed, N. M. Abbas, R. E. Jones, and D. S. Rickerby, *J. Mater. Sci.* **38**, 3797–3807 (2003).
35. C. M. Younes, G. C. Allen, and J. A. Nicholson, *Corrosion Engineering, Science and Technology* **42**, 2007 (80–88).
36. JMatPro: Ni module (Version 2.0), Sente Software, Guilford, UK, Nov. 2002.
37. C. L. Briant, W. H. Murphy, and J. C. Schaefer, *Scr. Metall. et Mater.* **32**, 1447–1451 (1995).